CAMBRIDGE
UNIVERSITY PRESS

**RESEARCH ARTICLE**

# Accurate kinematic and stiffness analysis of parallel cable-driven upper limb rehabilitation robot with spherical guide wheel cable-guiding mechanism

Yupeng Zou , Keyu Pan , Mengfei Wang , Xiaojing Lai, Tianyu Lan , Zhishen Zhou and Changsheng Li

College of Mechanical and Electrical Engineering, China University of Petroleum (East China), Qingdao, China
**Corresponding author:** Yupeng Zou; Email: zouyupeng@upc.edu.cn

**Abstract**

Cable-guiding mechanisms (CGMs) and the stiffness characteristics directly influence the dynamic features of the cable-driven upper limb rehabilitation robot (PCUR), which will affect PCUR's performance. This paper introduces a novel CGM design. Given the precision and movement stability considerations of the mechanism, an analytical model is developed. Using this model, we analyze the error of the CGM and derive velocity and acceleration mappings from the moving platform to the cables. Continuity of cable trajectory and tension is rigorously demonstrated. Subsequently, a mathematical model for PCUR stiffness is formulated. Utilizing MATLAB/Simscape Multibody, simulation models for the CGM and stiffness characteristics are constructed. The feasibility of the proposed CGM design is validated through simulation and experimentation, while the influence of stiffness characteristics on PCUR motion stability is comprehensively analyzed.

## 1. Introduction

Neurological disorders such as stroke have become a primary global concern, drawing attention to the urgent need for effective prevention, intervention, and rehabilitation strategies [14]. Current approaches to neurorehabilitation focus on task-specific repetitive movement practice, and there is growing interest in robotic approaches that assist the completion of movements and can enhance the effectiveness of the movement practice [5]. A large meta-analysis of 34 studies reported that using the upper limb rehabilitation robot had advantages over other interventions in promoting strength recovery and the ability to perform daily activities [6].

The cable used in rehabilitation robots has lower mass and rigidity and is superior to traditional rigid rehabilitation robots in terms of safety and flexibility control [7]. Parallel cable-driven robots (CDPRs)' inherent characteristics of speed, workspace, and carrying capacity make them suitable for a wide range of applications, such as rehabilitation, haptic interfaces, and outstanding radio telescopes [8]. They typically use redundant drive methods to achieve precise cable tension [9]. Damiano Zanotto proposed a 2-degree-of-freedom, fully constrained parallel cable-driven upper limb rehabilitation device [10] with a point-mass end-effector that employs three cables to reduce the possibility of mutual interference between the cable and the patient's limb. While seated in a chair, the patient interacts with the device by grasping the end-effector and receives visual feedback of the movement via a PC screen. Sui developed a cable-driven, soft-packaged, portable rehabilitation glove [11]. This glove utilizes five cables with front ends connected to shape memory alloy (SMA) actuators. The SMA actuators are linked to the finger joints, facilitating finger movement for rehabilitation training. Mohammed Khadem presents parallel cable-driven robots for exercising and resuming writing and drawing tasks with a special pyramid
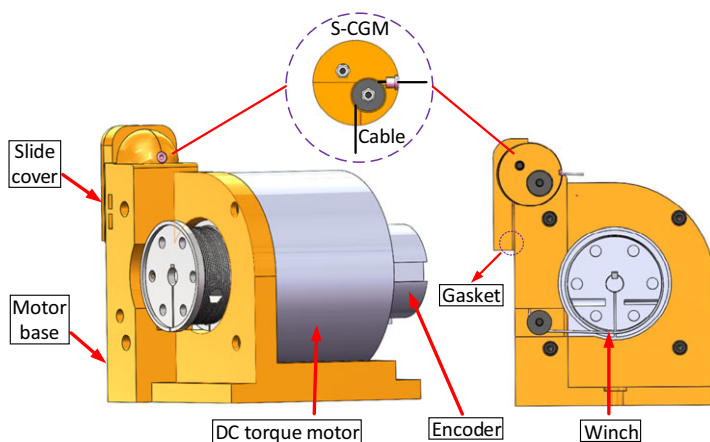
**Figure 1.** *Structure of cable-driven unit.*

topology and a compact footprint for home desks [12]. It employs a redundant drive with five flexible cables to allow for 3D point-to-point or continuous paths, and sliding mode control enables complex trajectory control of the end-effector. Zhang presented a flexible robot for transbronchial lung biopsy [13], which utilizes a flexible manipulator based on a cable-driven mechanism. The robot system is highly flexible and controllable, and the end effector is able to reach the target node by passing through a narrow and tortuous path. Alejandro Rodriguez-Barroso introduced RobUST [14], which utilizes eight cables connected to the human waist through end effectors to apply force to the body, stimulating the buoyancy environment when working underwater. Compared to the mechanisms described above, the mechanism designed in this paper is a six-degree-of-freedom upper limb rehabilitation robot driven by seven cables. The symmetric arrangement of the cable-driven units improves the robot's workspace, and the overall size of the robot eliminates restrictions on the patient's fixed position, facilitating the planning of various rehabilitation paths.

Cable-guiding mechanisms (CGMs) play a vital role in the cable-drive unit. The choice of CGMs affects the characteristics of PCUR, such as motion accuracy, motion continuity, motion stability, reconfigurability, and so on. Various kinematic structures for CGMs have been proposed and studied, with widely used mechanisms such as the eyelet [15–20] and pulley mechanism [21–25]. While eyelet-based CGM motion models are relatively straightforward and easy to analyze, they are susceptible to issues related to sliding friction and cable wear [26], making them unsuitable for applications requiring significant cable tension. On the other hand, the single-pulley-based CGM addresses the sliding friction problem but has limitations in cable orientations. Although this can be mitigated by restricting the mounting position of the CGM, it compromises reconfigurability. The dual-pulley-based CGM expands the cable's output angle range, yet the existence of its transition plane may lead to unsteady cable motion, potentially affecting PCUR motion. Additionally, the cable output point in pulley-based CGMs is not fixed, sacrificing some accuracy in motion control applications. To tackle these challenges, this paper introduces a novel composite guiding mechanism (CGM) based on a spherical guide wheel (S-CGM), as shown in Figure 1. The spherical guide wheel allows the cable to be output in multiple directions. The pulley system inside the spherical guide wheel reduces the cable's sliding friction. This mechanism can be seen as a CGM with a fixed output point at the center of the spherical wheel. Nonetheless, the S-CGM still has errors compared to the structure of the fixed-point output cable in the ideal case, so it is necessary to analyze its errors. In practice, the cable length based on S-CGM had demonstrated continuity. However, due to the complexity of the mechanism and the influence of the spherical joint, the actual motion is a complex composite motion, so it is unclear whether the cable length derivatives (e.g., velocity, acceleration, etc.) are also continuous and which higher-order derivative could this continuity be preserved. Therefore, it is necessary to investigate whether the cables' velocity, acceleration, and

tension are continuous, which is essential for exploring the continuity and stability of the rehabilitation motion of PCUR [27–30].

Furthermore, the stiffness characteristics of PCUR play a crucial role in determining the pose of the moving platform (MP). Tailoring appropriate stiffness can significantly enhance the stability and compliance of PCUR motion. In some cases, higher stiffness may provide more stable support and guidance, thereby assisting patients in performing movements more effectively. In other situations, lower stiffness may be more suitable for promoting joint flexibility and mobility. Verhoeven provided a stiffness analysis of a cable-driven Stewart platform manipulator [31], which shows that the stiffness of the manipulator is related to the cable stiffness and the pose of the MP. Cui introduced the concept of stiffness controllability for CDPR stiffness [32] and analyzed its local and global stiffness controllability. V. Ferravante, based on the linear finite element theory [33], discretized each cable of the CDPR into a finite element with a mass matrix and a stiffness matrix and carried out a theoretical analysis of the stiffness. However, while these studies primarily focus on theoretical analyses, there is limited research that integrates stiffness conditions with the actual motion of the robot. Further exploration is necessary to understand the impact of stiffness on the stability of PCUR motion.

The main contributions of this paper are as follows:

(1) The S-CGM is presented, and a model of S-CGM with analytic formulations is established. The error of the S-CGM compared to that of an ideal fixed-point output cable CGM has been analyzed, the mapping from the MP's trajectory to the cables' velocities and accelerations is provided, and the continuity of the velocity, acceleration, and tension of the cable is subsequently proven.

(2) The stiffness simulation model of PCUR is developed. The influence of stiffness on the motion stability of PCUR is concluded through simulation and experimentation.

The remainder of this paper is organized as follows. Section 2 introduces the PCUR structure and rehabilitation training form. Section 3 gives an accurate kinematic analysis based on S-CGM. Section 4 provides the theoretical analysis of PCUR stiffness and the establishment of the stiffness model. Section 5 describes the simulation results. Section 6 shows the experimental results. Finally, conclusions are drawn in Section 7.

## 2. Parallel cable-driven upper limb rehabilitation robot

### 2.1. Structure of the PCUR

The structure of the six-degree-of-freedom PCUR is shown in Figure 2. The PCUR consists of seven cable-driven units that move a retractable cable and traction a MP to drive the affected limb to perform rehabilitation. The patient sits on a rotating seat, the seat height is adjustable, and the patient's posture can be adjusted according to different rehabilitation modes. The PCUR has a simple configuration, which can meet different upper limb rehabilitation training modes.

The internal structure of the S-CGM, comprising a spherical housing, a pulley, ceramic eyes, and fasteners, is shown in Figure 3. When the output angle of the cable changes, the spherical wheel rotates accordingly, with the internal pulley rotating in tandem and aligning tangentially to the cable's output direction. The pulley is positioned specifically within the spherical wheel, such that the distance between the center of the pulley and the center of the spherical wheel is the square root of two times the pulley's radius. This design ensures that the output direction of the cable is always directed towards the center of the sphere so that the S-CGM approximates a fixed-point output compared to a pulley mechanism. In the position control of the PCUR, the pose of the MP is determined by the amount of change in the length of the cable, which is obtained by calculating the distance between the output point of the cable and the traction point. Therefore, the motion control accuracy can be improved by outputting the cable at a fixed point.

As shown in Figure 1, the cable-drive unit mainly consists of the S-CGM, side cover, motor base, winch, torque motor, and encoder. S-CGM setup enhances PCUR reconfigurability. On the one hand, due to the simple structure of the S-CGM and the fact that there is no need to add additional rotary joints,

(a)



(b)
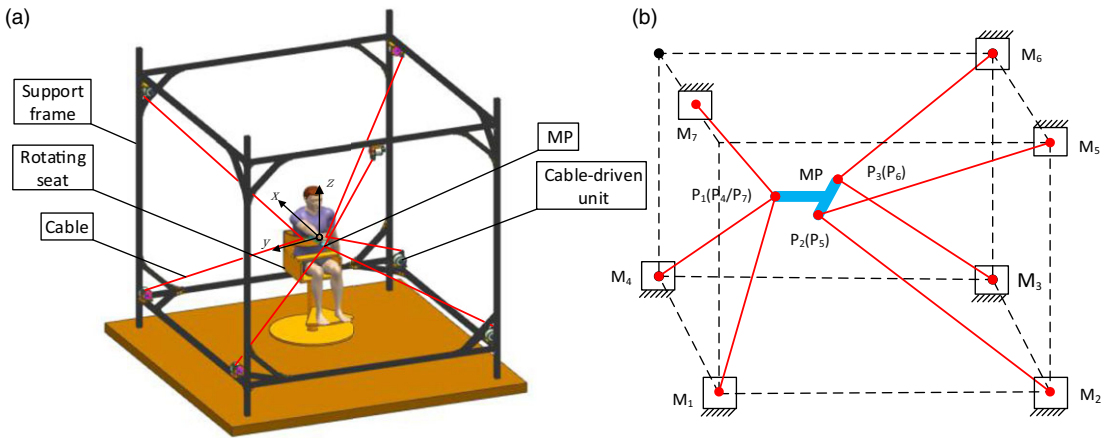
Figure 2. Structure of the PCUR: (a) Shows the structure of PCUR, and (b) Shows the schematic diagram of PCUR.
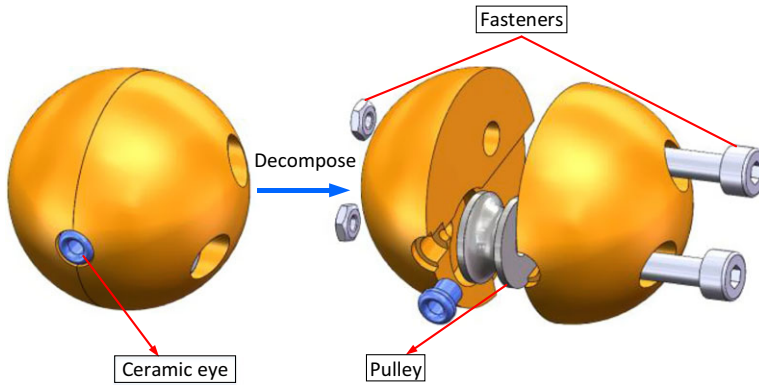


Figure 3. Decomposition view of S-CGM.

we can combine the cable-drive unit with the S-CGM in an integrated design. This design reduces the space required for installation and makes the system easier to install, adjust, and disassemble. Therefore, The cable-drive unit can be positioned on the profile frame anywhere in the PCUR and we can easily adjust the position of the tendril-driven unit. On the other hand, the presence of the spherical guide wheel enables the cable to be output in multiple directions and over a wide range, providing significant constraints between the mechanism and the cable. This ensures that even at extreme angles, the cable will not slip off.

This Section delves into issues related to friction, gaps, and vibrations within the mechanism. The S-CGM reduces the sliding wear of the cable in the following two ways: 1. The internal pulley of the S-CGM reduces the sliding wear on the cable. 2. The multi-degree-of-freedom rotation of the spherical wheel can mitigate the friction between the cable and the porcelain eye, thereby reducing sliding wear. Although there is friction between the spherical shell and the spherical groove, due to the strong constraint between the cable and the S-CGM, and the position control method mainly used in PCUR applications, the friction impact of the spherical vice is minimal. The S-CGM ensures that the spherical wheel rotates according to the direction of the cable exit. Additionally, we have placed adjustment an gasket between the side cover and the motor base; by changing the width of the gasket, the damping of the spherical wheel rotation can be altered. However, if the thickness of the gaskets is too large, it increases the gap between the spherical wheel and the spherical groove, which can cause vibrations
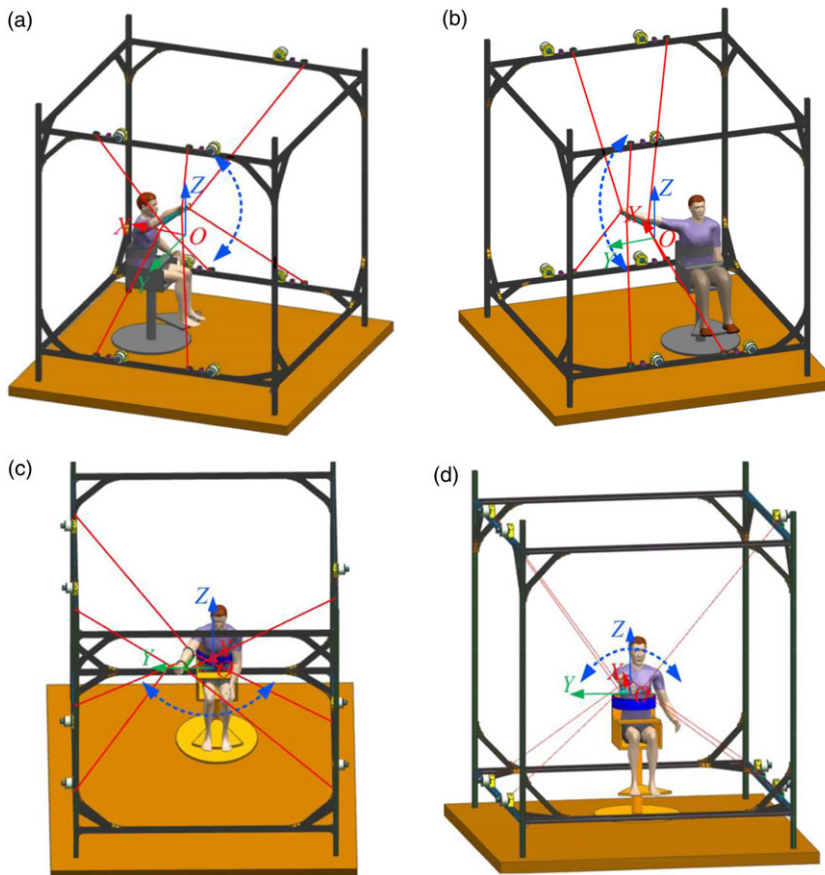
***Figure 4.*** *Forms of rehabilitation training.*

during the movement of the spherical wheel and affect motion stability. Therefore, the thickness of the gasket is set in the range of (1, 1.8) mm in this paper. With this configuration, the S-CGM experiences minimal vibration during actual movement, meeting the usage requirements.

## 2.2. PCUR-based forms of rehabilitation training

The upper limb rehabilitation training form is shown in Figure 4, where the neutral position is the starting position of the rehabilitation training: in (a), the shoulder joint's flexion/extension rehabilitation movement is demonstrated. In the middle position, the upper limb naturally drops and swings back and forth in the sagittal plane, resulting in the shoulder joint moving around the y-axis direction for shoulder rehabilitation. (b) shows the shoulder joint extension/retraction movement. Similar to the shoulder joint internal/external rotation rehabilitation movement, it causes the shoulder joint to rotate around the $x$-axis direction. (c) shows upper limb-shoulder-elbow joint extension movement. The neutral position resembles the shoulder joint extension/retraction rehabilitation movement. However, in the horizontal plane, the forearm of the upper limb swings back and forth, thus causing the elbow joint to move around the z-axis direction for elbow joint rehabilitation. (d) provides upper limb-shoulder-elbow joint internal/external rotation movement. In the neutral position, the right upper limb is straightened, the palm faces the body's side, and the upper limb's shoulder joint rotates around the x-axis direction.
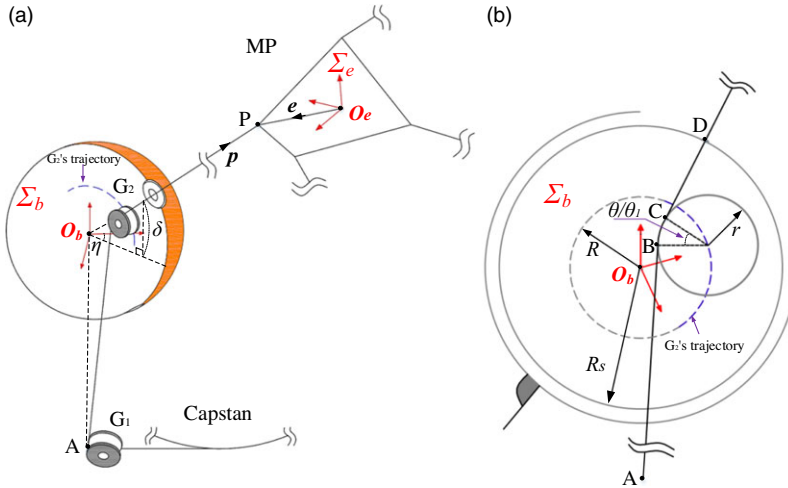
**Figure 5.** *S-CGM principle: (a) shows the S-CGM as a whole. (b) gives a detailed description of the S-CGM.*

## 3. Accurate kinematic analysis of S-CGM

### 3.1. S-CGM error analysis

Accurate kinematic modeling of PCUR based on S-CGM is shown in Figure 5. This paper focuses on the case of only one cable, and the other cables are analyzed similarly. Two coordinate frames are defined in Figure 5: static frame $\Sigma_b$ and the moving frame $\Sigma_e$. The origin of $\Sigma_b$ is $O_b$, which is the center of the sphere, and the origin $O_e$ of $\Sigma_e$ is the center of MP. According to the schematic diagram, the main function of pulley $G_1$ is to ensure that the cable is fed vertically upwards to the spherical guide wheel, and it also serves to tension the cable, and $G_2$ is the guide wheel fixed in the spherical guide wheel. The radius of both of them is $R_P = 5\,\text{mm}$ ($R_P$ considered here is the sum of the radius of the guide pulley and the radius of the cable, which can reduce the computational error), and the circle with $R_T$ as the radius denotes the trajectory of $G_2$ in the process of pitching and turning of the spherical guide wheel, and $R_T = \sqrt{2}R_P$. $R_S$ is the radius of the spherical shell.

During the simulation and analysis of PCUR, we typically treat the CGM as a structure with a fixed-point output to calculate the cable length for controlling the MP pose. Ideally, the volume of $G_2$ tends to be infinitesimal; at this time, the S-CGM motion model can be simplified to the model of the fixed-point input and output of the cable, as shown in Figure 6. In this scenario, the mechanism exhibits no error. However, in practical applications, although the S-CGM can ensure that the direction of the output of the cable is directed to the center of the sphere, the S-CGM still leads to a small error in the cable length compared to the ideal mechanism because the radius of $G_2$ cannot be zero. Since we consider the S-CGM as an ideal model when performing simulations and experiments, the existence of this error may affect the motion accuracy of PCUR. Therefore, the next step is to address this error.

Let $\boldsymbol{\xi} \in \boldsymbol{R}^6$ be the position of the center of the MP, that is, the pose of the MP. $\boldsymbol{q} = [q_1\ q_2\ q_3\ q_4\ q_5\ q_6\ q_7]^\text{T}$ denotes the lengths of the seven cables used to drive the PCUR. From the principle of robot kinematics, the mapping of the end pose to cable length is given by:

$$\boldsymbol{\xi}^T = \boldsymbol{J}^T \boldsymbol{q} \tag{1}$$

Where

$$\boldsymbol{J}^T = \left[ \left( \frac{\mathrm{d}q_1}{\mathrm{d}\boldsymbol{\xi}} \right)^T \left( \frac{\mathrm{d}q_2}{\mathrm{d}\boldsymbol{\xi}} \right)^T \cdots \left( \frac{\mathrm{d}q_7}{\mathrm{d}\boldsymbol{\xi}} \right)^T \right] \tag{2}$$

From Eq. (1), it can be seen that the length of each cable determines the pose of the MP of the PCUR. The presence of geometrical errors will lead to a deviation in the length of the cables, thus affecting the
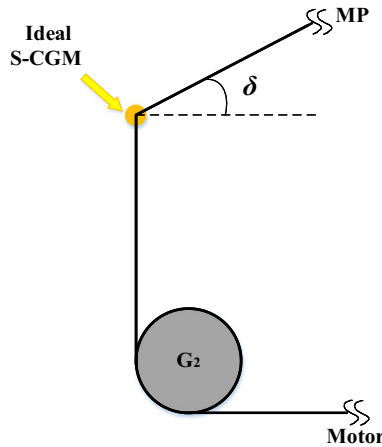
**Figure 6.** *Theoretical model of S-CGM in the ideal case.*

MP's pose. Defining the error of S-CGM as $\varphi$, then we have

$$\varphi = l_{O_bA} + l_{O_bB} - (l_{AB} + l_{BC}) \tag{3}$$

In Figure 5, $\delta$ and $\eta$ are the pitch angle and horizontal rotation angle of the spherical guide wheel, respectively; the coordinates of the center of $G_2$ are obtained as $(R_T\cos\delta\sin\eta, R_T\cos\delta\cos\eta, R_T\sin\delta)$, and the coordinates of point A are $(0, -l_0)$, where $l_0$ is a constant value, which yields

$$l_{AB} = \sqrt{(R_T{}^2 + 2R_T l_0 \sin\left(\delta - \frac{\pi}{4}\right) + l_0{}^2 - R_P{}^2} \tag{4}$$

We assume that the tangent point of the cable from $G_1$ to $G_2$ is the left quarter node of $G_2$, and the arc angle corresponding to the $l_{BC}$ at this time is $\theta$. In reality, the arc angle corresponding to $l_{BC}$ is $\theta_1$. Since the geometric relationship between $\theta_1$ and $\delta$ is not easy to determine, the calculation can be obtained as $\frac{|R_P\theta_1 - R_P\theta|}{r\theta} < 0.07$. Therefore, it can be approximated that $\theta_1 = \theta$, using $\theta$ to calculate the $l_{BC}$, we get:

$$l_{BC} = R_P\left(\frac{\pi}{2} - \delta\right) \tag{5}$$

$l_{O_bC} = R_P$ and $l_{O_bA} = l_0$. From this, $\varphi$ can be obtained as follows:

$$\varphi = R_P + l_0 - (\sqrt{\left(R_T{}^2 + 2R_T l_0 \sin\left(\delta - \frac{\pi}{4}\right) + l_0{}^2 - R_P{}^2} + R_P\left(\frac{\pi}{2} - \delta\right)) \tag{6}$$

To eliminate $\varphi$, the cable length compensation term can be added according to Eq. (1) as follows:

$$\boldsymbol{\xi}^T = \boldsymbol{J}^T \left[ q_1 + \Delta q_1 \cdots q_7 + \Delta q_7 \right]^T \tag{7}$$

where the compensation term $\Delta l_i = \varphi_i$, $\varphi_i$ is the geometric error generated by each S-CGM.

### 3.2. Mapping of MP posture to the length of the cable

In Figure 4, $\boldsymbol{p}$ is the position of the traction point on the MP, then we have:

$$\boldsymbol{p} = \left[x, y, z\right]^T = [\xi_1, \xi_2, \xi_3]^T + \boldsymbol{r} \tag{8}$$

where $[\xi_1, \xi_{[}2], \xi_{[}3]]^T$ are the first three sub-vectors of $\xi$ representing the position of MP. $\boldsymbol{r}$ represents the vector from the center of the MP to the tether attachment point and can be expanded as follows:

$$\boldsymbol{r} = \boldsymbol{R}\boldsymbol{e} \tag{9}$$

Where $\boldsymbol{R}$ is the rotation matrix from the local coordinate system $\Sigma_e$ to the global coordinate system $\Sigma_b$, and $\boldsymbol{e}$ is the position of the traction point on MP. Its position in $\Sigma_b$ is denoted by $\boldsymbol{p}$. Define the vector between the output of the cable-drive unit and the traction point as the tangent segment vector $\boldsymbol{l}$.

$$\boldsymbol{l} = \boldsymbol{p} - \boldsymbol{d} \tag{10}$$

where $\boldsymbol{d}$ is the vector from $O_b$ to point D. The cable leaves $G_2$ from point C through a constant cable length $l_{CD} = 12.5\,\text{mm}$, output by the ceramic eye. According to the geometrical relationship, it can be obtained:

$$\boldsymbol{d} = [R_S \cos\delta\sin\eta, R_S\cos\delta\cos\eta, R_S\sin\delta]^T \tag{11}$$

In addition to the tangent segment length, the cable length includes the length $l_{AB}$ between the $G_1$ and the spherical guide sheave and the arc segment $l_{BC}$ on the spherical guide sheave. Defining the length of the cable as $q$ and assuming that the plumpness of the cable is neglected, then

$$q = l_{AB} + l_{BC} + l_{CD} + ||\boldsymbol{l}|| \tag{12}$$

However, it is difficult to derive the velocity and acceleration of the cable by direct differentiation of a CGM based on a spherical guide wheel. Even with the help of computer algebra systems (e.g., maxima, mathematica, etc.), its differentiation produces extremely complex expressions that are not easy to simplify and difficult to use in analyses, and a solution to this problem is discussed below.

### 3.3. Velocity and acceleration equations for cables

For a given MP pose, the velocity and acceleration of the cable are:

$$\dot{q} = \frac{\mathrm{d}q}{\mathrm{d}\boldsymbol{\xi}}\dot{\boldsymbol{\xi}} \tag{13}$$

$$\ddot{q} = \dot{\boldsymbol{\xi}}^T \quad \boldsymbol{H}\dot{\boldsymbol{\xi}} + \frac{\mathrm{d}q}{\mathrm{d}\boldsymbol{\xi}}\ddot{\boldsymbol{\xi}} \tag{14}$$

Where $\boldsymbol{H}$ is the Hessian matrix of $q$ concerning $\boldsymbol{\xi}$, it can be expressed as:

$$\boldsymbol{H} = \frac{\mathrm{d}^2 q}{\mathrm{d}\boldsymbol{\xi}^2} \tag{15}$$

Let the cable tension be denoted by $\tau$, whose effect on the MP is denoted by the force/torque vector $\boldsymbol{F} \in \mathbb{R}^6$. Then get:

$$-\begin{bmatrix} \boldsymbol{u} \\ \boldsymbol{r}\times\boldsymbol{u} \end{bmatrix}\tau = \boldsymbol{F} \tag{16}$$

Where

$$\boldsymbol{u} = \frac{\boldsymbol{l}}{||\boldsymbol{l}||} \tag{17}$$

Where $\boldsymbol{u} = [u_{xi}, u_{yi}, u_{zi}]^T, \boldsymbol{l} = [l_x, l_y, l_z]^T$. Instead of the direct derivation of $q$, we use the principle of robot kinematics to obtain the differential relationship between the cable vector and the pose.

$$\frac{\mathrm{d}q}{\mathrm{d}\boldsymbol{\xi}} = -\left[\boldsymbol{u}^T, (\boldsymbol{r}\times\boldsymbol{u})^T\right] \tag{18}$$

By further differentiating Eq. (18), we can obtain the Hessian of $q$ as:

$$\boldsymbol{H} = \left[\left(\frac{\mathrm{d}\boldsymbol{u}}{\mathrm{d}\boldsymbol{\xi}}\right)^T, [\boldsymbol{r}]_\times\left(\frac{\mathrm{d}\boldsymbol{u}}{\mathrm{d}\boldsymbol{\xi}}\right)^T\right] + \left[0, \left(\frac{\mathrm{d}\boldsymbol{r}}{\mathrm{d}\boldsymbol{\xi}}\right)^T\right] \tag{19}$$

Where $[]_\times$ denotes the cross-product matrix of $R^3$ vectors and since

$$\frac{\mathrm{d}r}{\mathrm{d}\xi} = \left[0, -[r]_\times\right] \tag{20}$$

Only the expression $\mathrm{d}u/\mathrm{d}\xi$ in Eq. (19) needs to be simplified. It can be expressed as

$$
\begin{aligned}
\frac{\mathrm{d}u}{\mathrm{d}\xi} &= \frac{\mathrm{d}u}{\mathrm{d}l} \cdot \frac{\mathrm{d}l}{\mathrm{d}p} \cdot \frac{\mathrm{d}p}{\mathrm{d}\xi} = \frac{\mathrm{d}u}{\mathrm{d}l}\left(I - \frac{\mathrm{d}d}{\mathrm{d}p}\right)\frac{\mathrm{d}p}{\mathrm{d}\xi} \\
&= \frac{\mathrm{d}u}{\mathrm{d}l} \cdot \frac{\mathrm{d}p}{\mathrm{d}\xi} - \frac{\mathrm{d}u}{\mathrm{d}l} \cdot \frac{\mathrm{d}d}{\mathrm{d}(\delta, \eta)} \cdot \frac{\mathrm{d}(\delta, \eta)}{\mathrm{d}(\rho, z, \eta)} \cdot \frac{\mathrm{d}(\rho, z, \eta)}{\mathrm{d}p}
\end{aligned} \tag{21}
$$

Decomposing the vectors $u$ and $l$ yields that $u = [u_x, u_y, u_z]^T$ and $l = [l_x, l_y, l_z]^T$. For the other components in Eq. (21), one gets

$$\frac{\mathrm{d}u}{\mathrm{d}l} = \frac{l^T l I - l l^T}{||l||^3} = \frac{1}{||l||^3}
\begin{bmatrix}
l_y^2 & -l_x l_y & 0 \\
-l_x l_y & l_x^2 & 0 \\
0 & 0 & l_x^2 + l_y^2
\end{bmatrix} \tag{22}$$

$$\frac{\mathrm{d}p}{\mathrm{d}\xi} = \left[I, -[Re]_\times\right] \tag{23}$$

$$\frac{\mathrm{d}(\rho, z, \eta)^T}{\mathrm{d}p} =
\begin{bmatrix}
\dfrac{x}{\rho} & \dfrac{y}{\rho} & 0 \\
0 & 0 & 1 \\
\dfrac{y}{\rho^2} & \dfrac{-x}{\rho^2} & 0
\end{bmatrix} \tag{24}$$

Where

$$\rho = \sqrt{x^2 + y^2} \tag{25}$$

Similarly, we can get

$$\frac{\mathrm{d}(\delta, \eta)^T}{\mathrm{d}(\rho, \eta, z)^T} =
\begin{bmatrix}
-\dfrac{z}{z^2 + \rho^2} & 0 & \dfrac{\rho}{z^2 + \rho^2} \\
0 & 1 & 0
\end{bmatrix} \tag{26}$$

$$\frac{\mathrm{d}d}{\mathrm{d}(\delta, \eta)^T} =
\begin{bmatrix}
R_s c_\delta & -R_s s_\delta s_\eta & -R_s s_\delta c_\delta \\
0 & R_s c_\delta c_\eta & -R_s c_\delta s_\eta
\end{bmatrix}^T \tag{27}$$

Where $s_\delta$, $s_\eta$, $c_\delta$ and $c_\eta$ represent $\sin\delta$, $\sin\eta$, $\cos\delta$ and $\cos\eta$.

All the components in Eq. (21) have been expressed in terms of the expansion of Eqs. (22)-(27), and finally, the cable's length, velocity, and acceleration can be obtained given the trajectory of the MP.

### 3.4. Continuity of speed, acceleration, and tension of cables

With the closed-form expression of cable acceleration, the continuity of cable trajectory can be analyzed. The analytical expression of acceleration has been given in the previous subsection. Let's first analyze the continuity of the most complicated component $\mathrm{d}u/\mathrm{d}\xi$.

The workspace of PCUR is obtained from this method as Figure 7 and Figure 8. Due to the limitation of the workspace, there will not be a situation where $O_e$ is close to $O_b$ during PCUR's operation, so the $x$ and $y$ will not be zero at the same time, and therefore $\rho$ will not be zero. Consequently, the elements within each component matrix exhibit continuity without any discontinuity points.
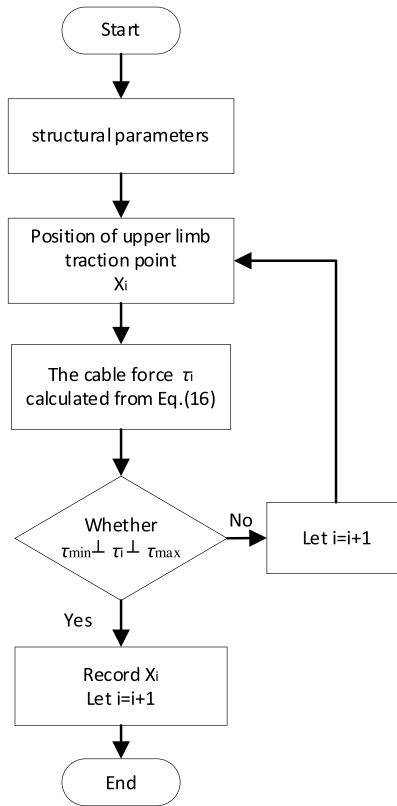
**Figure 7.**  *Workspace-solving process for PCUR.*
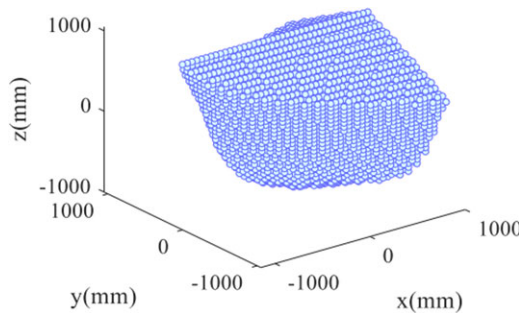


**Figure 8.**  *PCUR's workspace.*

Therefore, all individual components of $du/d\xi$.maintain a state of continuity. According to the rules of arithmetic operations for continuous functions, it can be deduced that the sum and product of continuous functions are both continuous. Thus, the continuity can be testified.

(1) As $du/d\xi$ is continuous, in accordance with the property that the integral of a continuous function is continuous, it follows that $u$ is continuous. Therefore, in line with Eq. (18), we can deduce that $dq/d\xi$ is continuous.

(2) Due to the continuity of Eq. (20) and Eq. (21), it can be inferred that the Hessian matrix is continuous.

(3) Due to the continuity of $dq/d\xi$, according to Eq. (13), it can be concluded that $\dot{q}$ is continuous. Therefore, the velocity of the cable is continuous. Furthermore, according to Eq. (14), it can be deduced

that $(\ddot{q})$ is continuous since the Hessian matrix is continuous. Consequently, the acceleration of the cable is continuous.

The continuity of cable tension, in addition to the continuity of cable trajectories, is equally crucial for an in-depth analysis of PCUR [34–37]. Defining $\boldsymbol{\tau} = [\tau_1, \tau_2, \tau_3, \tau_4, \tau_5, \tau_6, \tau_7]^T$ to denote the force of the seven cables, and referring to Eq. (16), we have:

$$\boldsymbol{\tau} = -\left(\boldsymbol{J}^T\right)^+ \boldsymbol{F} + \lambda \boldsymbol{N} \tag{28}$$

And $\boldsymbol{\tau}$ needs to meet the following condition:

$$0 \leq \tau_{\min} \leq \tau_i \leq \tau_{\max} \tag{29}$$

Regarding Eqs. (28–29), $(\boldsymbol{J}^T)^+$ is the pseudo-inverse matrix of the structure matrix $\boldsymbol{J}^T$, $\boldsymbol{F} \in \boldsymbol{R}^6$ is the total external force/torque exerted on MP, $\boldsymbol{N}$ is the nulling space of $\boldsymbol{J}^T$, $\lambda$ is an arbitrary nonzero constant, and $\tau_{\max}$ and $\tau_{\min}$ respectively represent the maximum cable tension and minimum cable tension.

The proof of cable tension continuity under the constraints of Eq. (28) and Eq. (29) is mainly divided into two parts:

① $\boldsymbol{J}$ concerning $\boldsymbol{\xi}$ is continuous.

② $\boldsymbol{\tau}$ concerning $\boldsymbol{J}$ is continuous.

For ①, as previously demonstrated in the preceding text, $\boldsymbol{J}$ is continuous. For ②, numerous methods have been proposed to compute $\boldsymbol{\tau}$ with guaranteed continuity (refer to [36] for details). At this point, it can be theoretically demonstrated that the cables' velocity, acceleration, and tension are based on S-CGM.

## 4. Establishment of PCUR static stiffness analysis and simulation model

The stiffness of PCUR is also a critical factor influencing its performance. To further ensure the stability of MP movement during rehabilitation training, we will analyze the composition of PCUR stiffness.

The ability of MP to resist changes in position under external forces is an essential indicator for determining the stiffness of rehabilitation robots. Therefore, stiffness can be expressed by the relationship between small external force $d\boldsymbol{F}$ and the resulting small positional change $d\boldsymbol{\xi}$ as follows:

$$d\boldsymbol{F} = \boldsymbol{K} \cdot d\boldsymbol{\xi} \tag{30}$$

$\boldsymbol{K}$ is the static stiffness matrix, $\boldsymbol{K} \in \boldsymbol{R}^{6 \times 6}$, obtained from Eq. (16) and Eq. (30).

$$\boldsymbol{K} = \frac{d\boldsymbol{F}}{d\boldsymbol{\xi}} = -\left(\frac{d\boldsymbol{J}^T}{d\boldsymbol{\xi}} \boldsymbol{\tau} + \boldsymbol{J} \frac{d\boldsymbol{\tau}}{d\boldsymbol{\xi}}\right) = \boldsymbol{K}_T + \boldsymbol{K}_S \tag{31}$$

$\boldsymbol{K}_T$ is the MP pose stiffness, and $\boldsymbol{K}_S$ is the cable pose stiffness. The following derivation of $\boldsymbol{K}_T$ and $\boldsymbol{K}_S$ is carried out:

$$\boldsymbol{K}_T = -\frac{d\boldsymbol{J}^T}{d\boldsymbol{\xi}} \boldsymbol{\tau} = -\boldsymbol{W}\boldsymbol{\tau} \tag{32}$$

Where $\boldsymbol{W}$ is

$$\boldsymbol{W} = \frac{d\boldsymbol{J}^T}{d\boldsymbol{\xi}} = \begin{bmatrix} \dfrac{d\boldsymbol{u}_1}{d\boldsymbol{\xi}} & \dfrac{d\boldsymbol{u}_2}{d\boldsymbol{\xi}} & \cdots & \dfrac{d\boldsymbol{u}_7}{d\boldsymbol{\xi}} \\[3mm] \dfrac{d\left(\boldsymbol{r}_1 \times \boldsymbol{u}_1\right)}{d\boldsymbol{\xi}} & \dfrac{d\left(\boldsymbol{r}_2 \times \boldsymbol{u}_2\right)}{d\boldsymbol{\xi}} & \cdots & \dfrac{d\left(\boldsymbol{r}_7 \times \boldsymbol{u}_7\right)}{d\boldsymbol{\xi}} \end{bmatrix} \tag{33}$$

Where $\boldsymbol{u}_i$ is the unit vector of the ith cable. $\boldsymbol{r}_i$ denotes the vector from the center of MP to the connection point of the ith cable. To solve for each component in $\boldsymbol{W}$, the first step is to solve for $d\boldsymbol{u}_i/d\boldsymbol{\xi}$.

The slight change in the cable unit vector is obtained as

$$d\boldsymbol{u}_i = \overline{\boldsymbol{u}}_i - \boldsymbol{u}_i = \frac{\overline{\boldsymbol{l}}_i}{\overline{l}_i} - \frac{\boldsymbol{l}_i}{l_i} \tag{34}$$
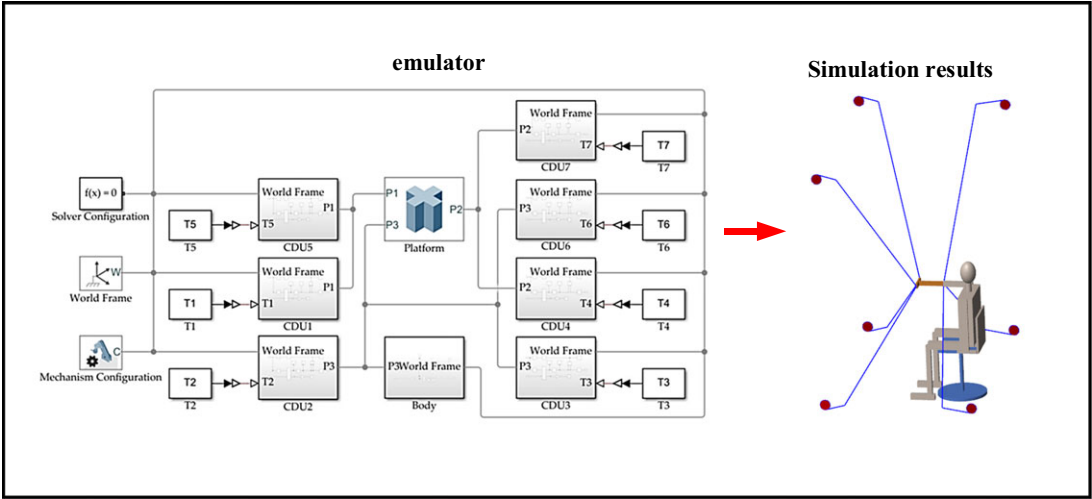
**Figure 9.** *Stiffness simulation model of PCUR.*

Where $\bar{l}_i$ and $l_i$ are the ith cable vectors before and after the displacement occurs. Similarly, the ith cable unit vector is changed from $\bar{u}_i$ to $u_i$.

Then

$$\frac{du_i}{d\xi} = \frac{1}{l_i} \begin{bmatrix} u_{xi}^2 - 1 & u_{xi}u_{yi} & u_{xi}u_{zi} \\ u_{yi}u_{xi} & u_{yi}^2 - 1 & u_{yi}u_{zi} \\ u_{zi}u_{xi} & u_{zi}u_{yi} & u_{zi}^2 - 1 \end{bmatrix} \tag{35}$$

Next, solve for $d(r_i \times u_i)/d\xi$:

$$\frac{d(r_i \times u_i)}{d\xi} = \frac{dr_i}{d\xi} \times u_i + r_i \times \frac{du_i}{d\xi} \tag{36}$$

Since $dr_i/d\xi$ can be obtained from Eq. (20), the analytical expression for $d(r_i \times u_i)/d\xi$ can be derived. Next, solve for the cable pose stiffness $K_S$:

$$K_S = J^T \cdot diag\left(\frac{E_1 \cdot A_1}{q_1}, \frac{E_2 \cdot A_2}{q_2}, \cdots \frac{E_7 \cdot A_7}{q_7}\right) \cdot J \tag{37}$$

Where $E_i$ is the flexure modulus of the cable, $A_i$ is the cross-sectional area of the cable, $q_i$ is the length of the cable.

Here, the static stiffness matrix of PCUR has been solved. The stiffness simulation model is established in MATLAB/Simscape Multibody, as shown in Figure 9. Seven cable-drive units are connected to the three traction points of the MP and have inputs with defined torque values to keep the MP stationary.

## 5. Simulation results

### 5.1. Simulation analysis of S-CGM

To analyze the accuracy of S-CGM, this paper establishes the simulation model of CGM based on single/double pulleys and S-CGM based on Matlab Simcape/Multibody as shown in Figures 10-12, in which the radius of the single/double pulleys is the same as that of the $G_2$, and the radius of the winches as well as the initial position of the end-effector are kept the same.

The coordinates of the ideal fixed point are set to (0, 0, 0), and the initial coordinates of the end-effector are set to (30, 0, 0). Given the trajectory of the end-effector, the dynamic cable length errors of different CGMs compared to the ideal fixed-point output guiding mechanism are analyzed as the angle
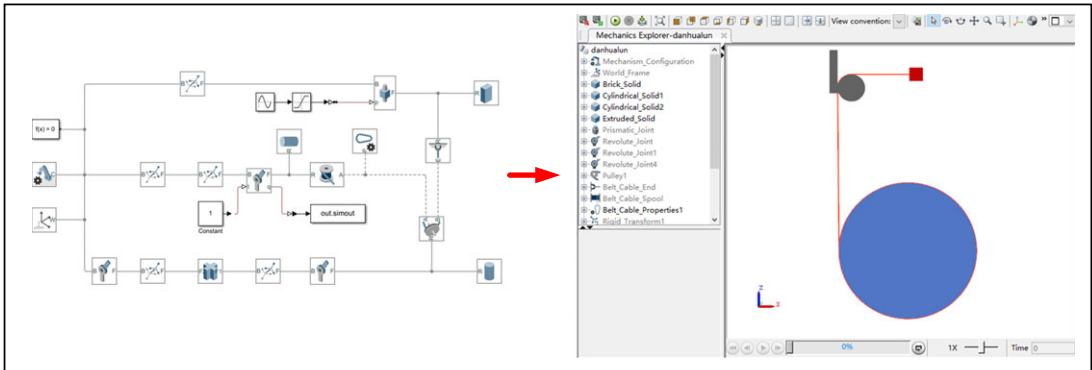
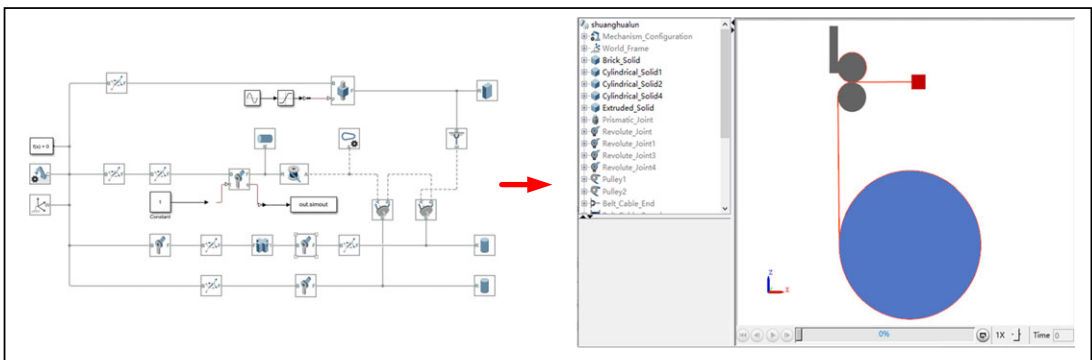**Figure 10.** *Model of a single pulley.*



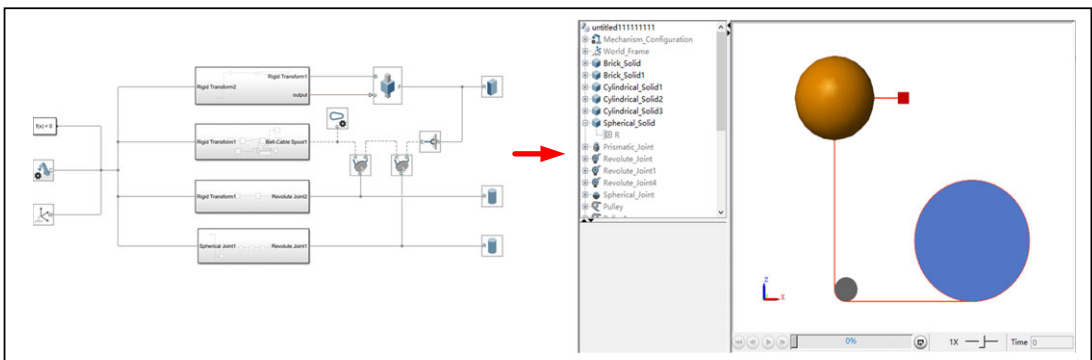**Figure 11.** *Model of a double pulley.*



**Figure 12.** *Model of the S-CGM.*

of rotation $\delta$ grows from 0 to $\pi/2$. According to Eq. (6), $\varphi$ is the determining factor that affects the change in error. The CGM based on the eyelet mechanism can approximate the ideal fixed-point output CGM when the eyelet radius is close to the cable radius, but it tends to cause greater wear and tear on the cable. Therefore, the error analysis of the eyelet-based CGM is not simulated. Based on the simulation model, we analyze the errors of single/double pulley-based CGMs and the S-CGM, as shown in Figure 13. Comparative analysis reveals that the error of the S-CGM is generally smaller compared to the error of pulley-based CGMs. Furthermore, because the direction vectors of the output of the cable by the S-CGM always pass through the ideal fixed point, the error under the S-CGM remains unchanged as the
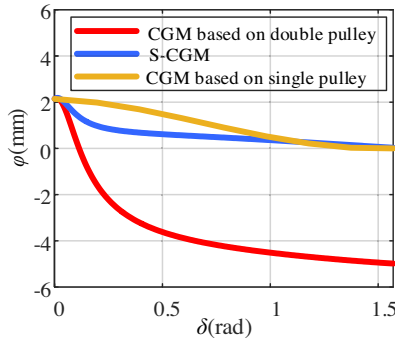
**Figure 13.** *Errors in single/double pulley-based CGM and S-CGM.*
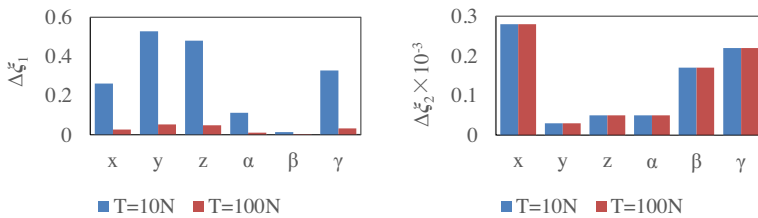


**Figure 14.** *Demonstrates the data comparison of MP pose changes caused by $K_S$ and $K_T$ for a given $F$ and increasing $\tau$.*

cable lengths vary with $\delta$. In contrast, the pulley-based CGM is affected by this variation, necessitating compensation terms that are challenging to incorporate into actual control. From the simulation data of the S-CGM, it is observed that the maximum cable error is 2.14 mm at $\delta = 0$, with a relative error of 2.7%. The minimum error is 0 mm, occurring at $\delta = \pi/2$. Thus, the cable length error generated by the S-CGM is minimal, closely approximating the ideal model. Moreover, the error of the S-CGM can be mitigated by applying cable length compensation through Eq. (7).

### 5.2. Simulation analysis of PCUR stiffness characteristics

According to Eq. (30), if the external load and stiffness are known, the pose change can be obtained as

$$\Delta \boldsymbol{\xi} = \boldsymbol{K}^{-1} \cdot \boldsymbol{F} \tag{38}$$

Take the MP center point located at $\boldsymbol{\xi} = [0, 0, 0, 0, 0, 0]^T$ position as an example to analyze the relationship between the amount of pose change and the MP position stiffness $\boldsymbol{K}_T$ and the cable position stiffness $\boldsymbol{K}_S$. Under a particular load, the pose change generated by $\boldsymbol{K}_T$ is set to be $\Delta \boldsymbol{\xi}_1$, and the pose change generated by $\boldsymbol{K}_S$ is set to be $\Delta \boldsymbol{\xi}_2$.

Firstly, the external load force $\boldsymbol{F} = [10, 10, 10, 0, 0, 0]^T$ is unchanged, and the changes of $\Delta \boldsymbol{\xi}_1$ and $\Delta \boldsymbol{\xi}_2$ are shown in Figure 14, given that the cable tension is $\boldsymbol{\tau} = [10, 10]^T$ and $\boldsymbol{\tau} = [100, 100, 100, 100, 100, 100, 100]^T$, respectively.

When the $\boldsymbol{\tau}$ is enlarged by ten times, $\Delta \boldsymbol{\xi}_1$ is correspondingly shrunk by ten times, which indicates that the pose change of MP induced by the $\boldsymbol{K}_T$ is inversely proportional to the cable tension, which also indicates that the $\boldsymbol{K}_T$ is proportional to the cable tension, verifying the theory of Eq. (31). $\Delta \boldsymbol{\xi}_2$ is unchanged, indicating that $\boldsymbol{K}_S$ is independent of the magnitude of the cable tension. The comparison of the two figures shows that the influence of $\boldsymbol{K}_T$ and $\boldsymbol{K}_S$ on the pose of MP at a given cable tension is not in order of magnitude. $\boldsymbol{K}_T$ is the main factor, while the influence of $\boldsymbol{K}_S$ is almost negligible.

**Table I.** *Positions of cable-drive unit.*

| serial number | positions |
|---|---|
| $S_1$ | $[-1.083, -1.318, -1.055]$ |
| $S_2$ | $[1.083, -1.318, -1.055]$ |
| $S_3$ | $[1.083, 1.318, -1.055]$ |
| $S_4$ | $[-1.083, 1.318, -1.055]$ |
| $S_5$ | $[1.083, -1.318, 1.055]$ |
| $S_6$ | $[1.083, 1.318, 1.055]$ |
| $S_7$ | $[-1.285, 0, 1.055]$ |

**Table II.** *PCUR's parameters.*

| parameters | value |
|---|---|
| MP mass | 1.556 kg |
| $R_P$ | 4.5 mm |
| $R_S$ | 17.5 mm |
| $R_T$ | 6.3 mm |
| 3D dimensions of PCUR | 2.4 m × 2.4 m × 2.4 m |
| Minimum cable tension($\tau_{min}$) | 10N |
| Maximum cable tension($\tau_{max}$) | 200N |
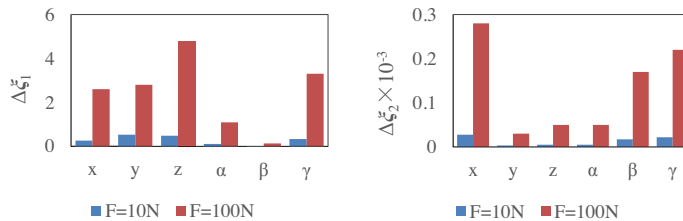


**Figure 15.** *Demonstrates the comparison of the data of MP pose changes caused by $K_S$ and $K_T$ for a given $\tau$, increasing $F$.*

When $\tau = [10, 10, 10, 10, 10, 10, 10]^T$ is given, so that when $F = [10, 10, 10, 0, 0, 0]^T$ and $F = [100, 100, 100, 0, 0, 0]^T$ are taken, respectively, the changes of $\Delta\xi_1$ and $\Delta\xi_2$ are shown in Figure 15.

It can be seen that when the $F$ is increased by ten times, both $\Delta\xi_1$ and $\Delta\xi_2$ are enlarged by ten times, so the amount of pose change is directly proportional to the external load. Under both conditions of given $F$ and given $\tau$, the pose change caused by $K_S$ is minimal. Therefore, planning different ranges of cable tension can create different stiffness conditions of PCUR.

## 6. Experimental results

### 6.1. Introduction to the experimental platform

The S-CGM's installed positions are given in Table I and the other parameters of the PCUR are shown in Table II, where $S_i$ refers to the ith S-CGM. The range of values for the tension of the cable is determined by the minimum preload and the maximum tension that the cable can withstand, which is related to the intensity of the rehabilitation exercise.

The semi-physical simulation experimental platform consists of an upper computer and a real-time simulation unit. The upper computer runs on the Windows operating system and is equipped with MATLAB and RT-SIM software. The real-time simulation unit, Links, runs on the VxWorks real-time
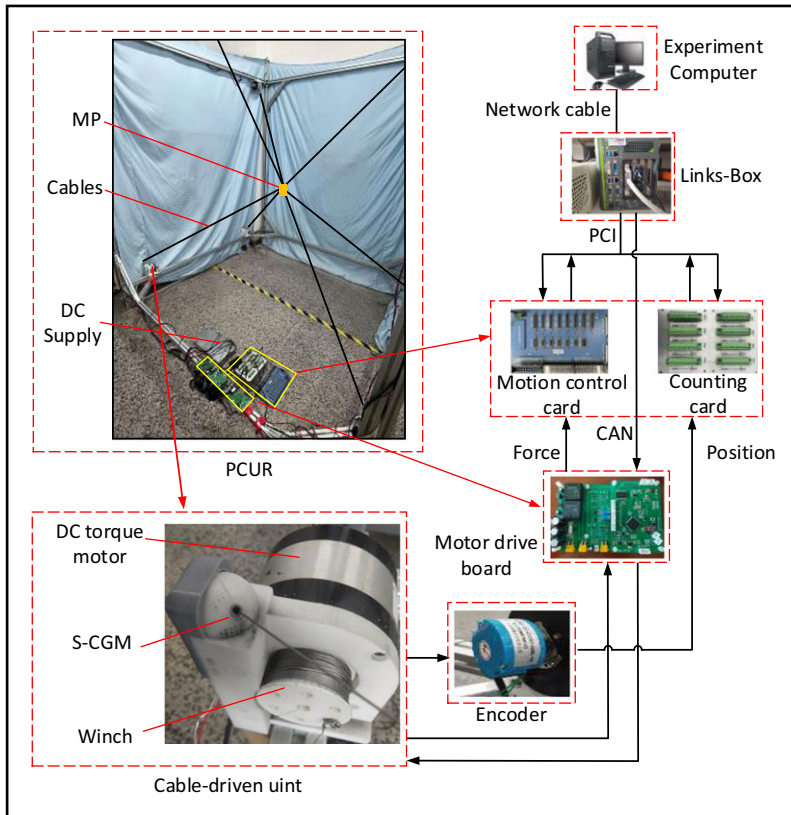
***Figure 16.***   *Experiment platform.*

operating system and is equipped with CAN cards, counter cards, and motion control cards. It is connected to external devices via the CAN and PCI buses for encoder data acquisition and analog signal acquisition. The experiment utilizes seven permanent magnet DC torque motors. One end of each motor is a winch for winding cables, while the other is equipped with an encoder to collect motor rotation data. The encoder allows for the determination of the respective changes in the length of each cable. The motor driver is a self-designed motor driver capable of collecting current data during the rotation of permanent magnet DC torque motors, and calibration experiments for the relationship between force and current for each motor have been completed. Combining the rotation data collected by the encoder with the current data obtained by the motor driver enables the acquisition of position and force feedback information, thereby achieving closed-loop control of the PCUR. The process is shown in Figure 16.

### 6.2. Verification of the continuity of the trajectory and tension of the cable

The following experiments verified the trajectory of the cable. Considering that full rotation of the spherical guide wheel is not easy to achieve when controlling the position of the MP in the workspace of the PCUR. We use two cables to connect to the MP, manually giving the MP motion to let the spherical guide wheel rotate fully. The feedback pulse count collected by the encoder can be used to calculate the cable length, and the results are shown in Figure 17, where $l_1$ and $l_2$ in (a) and $v_1$ and $v_2$ in (b) and $a_1$ and $a_2$ in (c) denote the length, velocity, and acceleration of cable 1 and cable 2, respectively. We can observe that the lengths and velocities of the cables are continuous. However, the acceleration of the
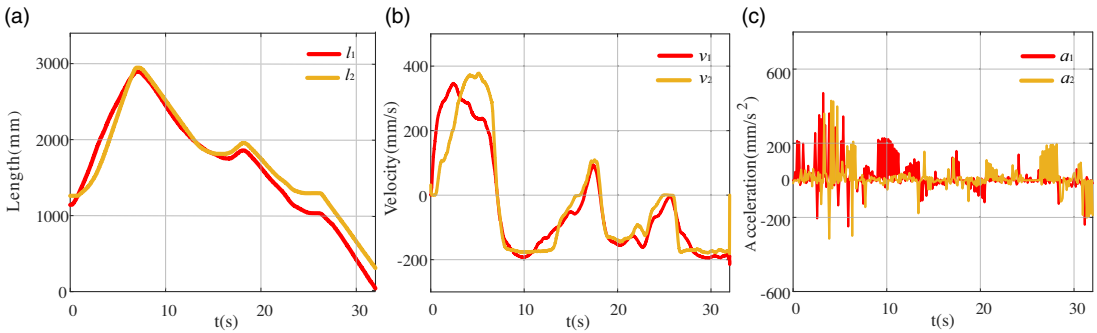
**Figure 17.** *Cable trajectories correspond to the S-CGM, where (a) shows the length of the cable, (b) shows the velocity of the cable, and (c) shows the acceleration of the cable.*
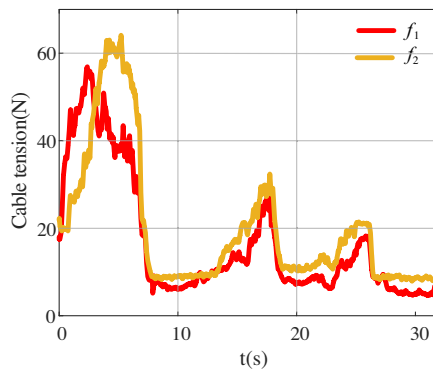


**Figure 18.** *Cable tension corresponds to the S-CGM.*

cables exhibits considerable noise due to the necessity of estimating its actual value through the second-order differentiation of the cable length. Therefore, the numerical values of acceleration lack reference significance, but their continuity is present.
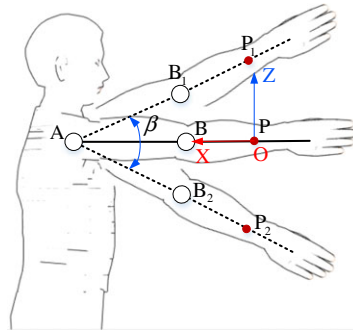
The tensions of the cable 1 as well as the cable 2 are denoted as $f_1$ and $f_2$, respectively, as shown in Figure 18, and it can be seen that the tension of the two cables is continuous during the experiment. This also indicates that the drive torque is not intermittent or stuttering. In the actual passive rehabilitation training of the upper limb, it is necessary to control the pose of the MP. At this juncture, employing a reasonable planning algorithm for cable tension can ensure the continuity of the cable tension.

According to these results, The S-CGM ensures the continuity of cable length, velocity, acceleration, and tension in the output, providing a reliable guarantee for the continuity and stability of the trajectory in PCUR operations.

### 6.3. Verification of PCUR rehabilitation training trajectory continuity based on S-CGM

According to the average data of human upper limb length, take the upper arm length $a_1 = 313$ mm, and forearm length $a_2 = 237$ mm. The movement trajectory of the shoulder joint flexion and extension rehabilitation is given as Eq. (38), and the parameter is shown in Figure 19.

$$\begin{cases} \beta = \frac{20\pi}{180} \sin\left(\frac{\pi}{3}t\right) \\ x = -\left(a_1 + \frac{a_2}{2}\right)(\cos\beta - 1) \ \ 0 \le t \le 6 \ (\text{s}) \\ z = \left(a_1 + \frac{a_2}{2}\right)\sin\beta \end{cases} \tag{39}$$

**Figure 19.** *A kinematic model describing the spreading and retracting motion of the human shoulder joint.*
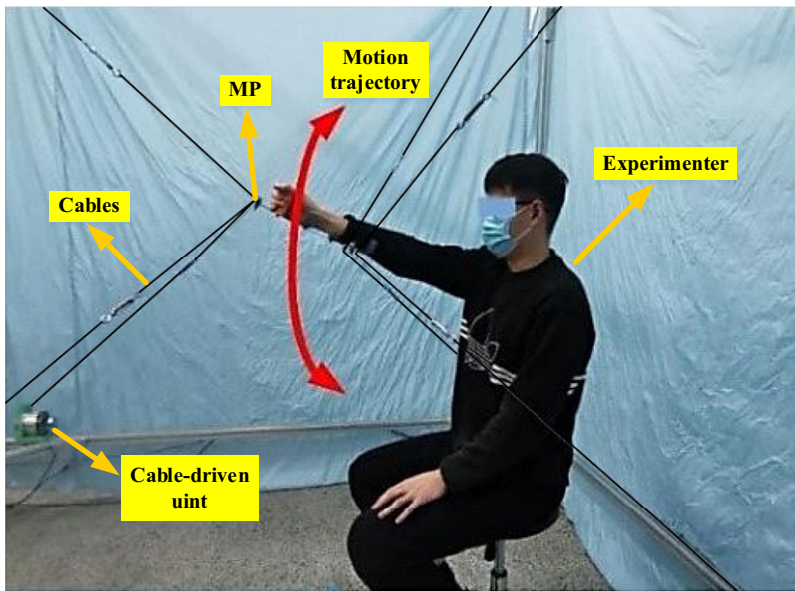


**Figure 20.** *Shoulder spreading and retracting man-robot experiment..*

The given MP trajectory is the O-point trajectory. The position of the S-CGM can be obtained from the expected cable length combined with the impedance control drive PCUR. The experimental process is shown in Figure 20, and the experimental results are obtained as shown in Figure 21 where the blue line represents the actual cable length/trajectory and the red dashed line represents the desired cable length trajectory.

The given MP trajectory is the O-point trajectory. the position of S-CGM can be derived from the expected cable length. Here we use the minimum variance algorithm [37] to plan the tension of the cable and combine it with impedance control for the shoulder flexion/extension movement. The experimental procedure is shown in Figure 20, and the experimental results are shown in Figure 21, where the blue line represents the actual cable length/trajectory and the red dashed line represents the desired cable length trajectory.

(a)~(g) show the comparison between the expected and actual values of the length change of the cable $1 \sim 7$, where $x_{di}$ represents the desired length change of the ith cable and $x_i$ represents the actual length change of the ith cable, respectively. The error between the actual cable length change and the
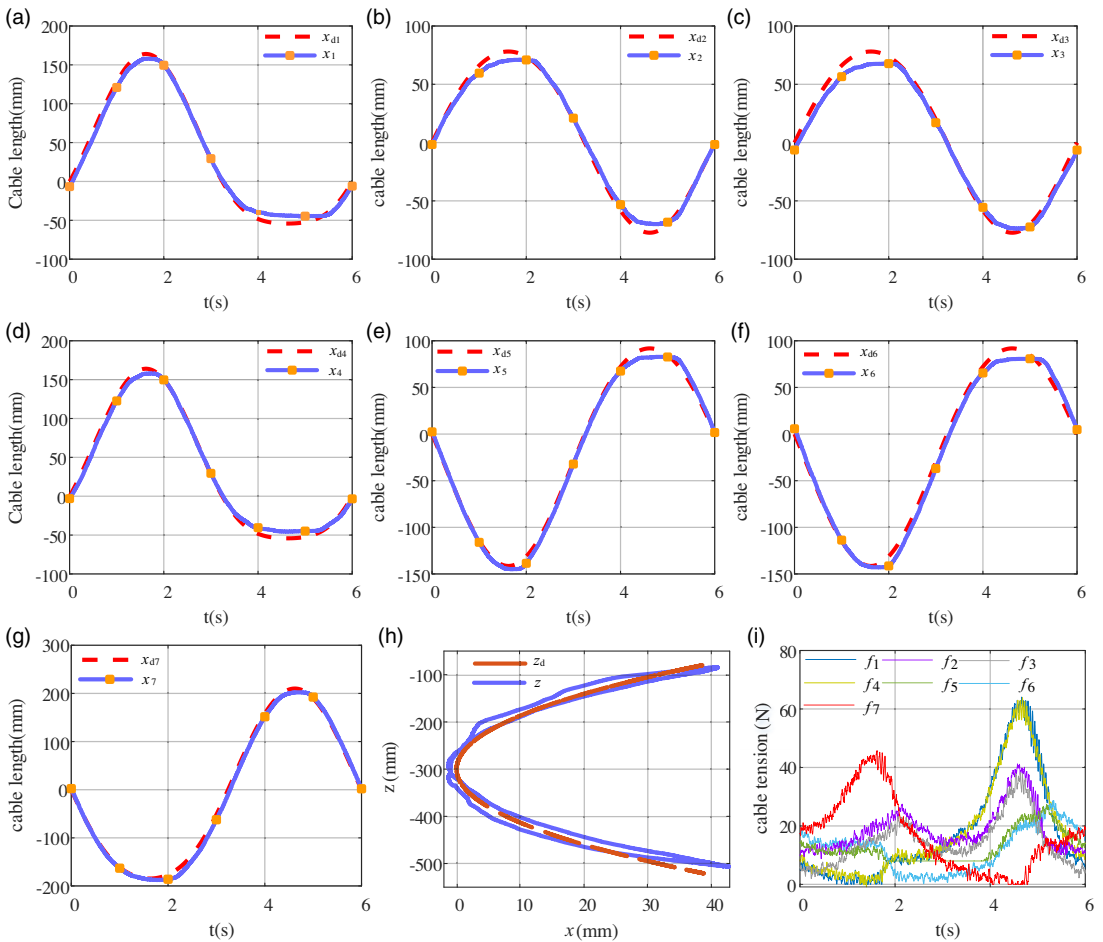
**Figure 21.** *Experimental data of MP running shoulder flexion and extension motion trajectory.*

expected cable length change is around $\pm 10$ mm, with a relative error of 0.67%. (h) shows the comparison between the expected trajectory of the center point of the movable platform and the actual trajectory, where $z_d$ denotes the expected value of $z$. We can see that the position and angle of $z$ can follow the given expected trajectory. The trajectory fluctuates slightly due to the oscillations of the MP in the movement process, but it generally meets the requirements of upper limb rehabilitation training. (i) shows the variation of the tension of seven cables, where $f_i$ represents the tension of the ith cable. It can be seen that the cable tensions are all continuous, again confirming the conclusion in 6.2. Thus, we have verified that the PCUR based on S-CGM can realize the spreading and retracting motion of the shoulder joint of the upper limb and has a continuous and smooth motion trajectory. In practice, PCUR can also be used for other rehabilitation training.

### 6.4. The effect of stiffness on the stability of MP motion

To explore the impact of $F$ on the stability of PCUR motion, we conducted experiments to investigate the relationship between the variation in cable length and the $F$ under different stiffness conditions, as follows: At the initial state, the MP is positioned at the zero point, with one person holding a fixed weight. The weight is connected to the motion platform, and upon release, it falls freely, as illustrated in Figure 22. The experiments were conducted under three different stiffness conditions: low, medium, and
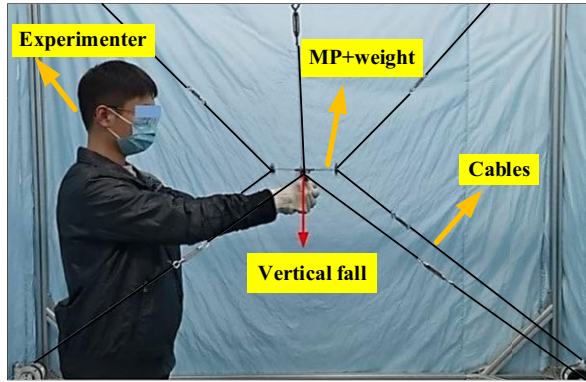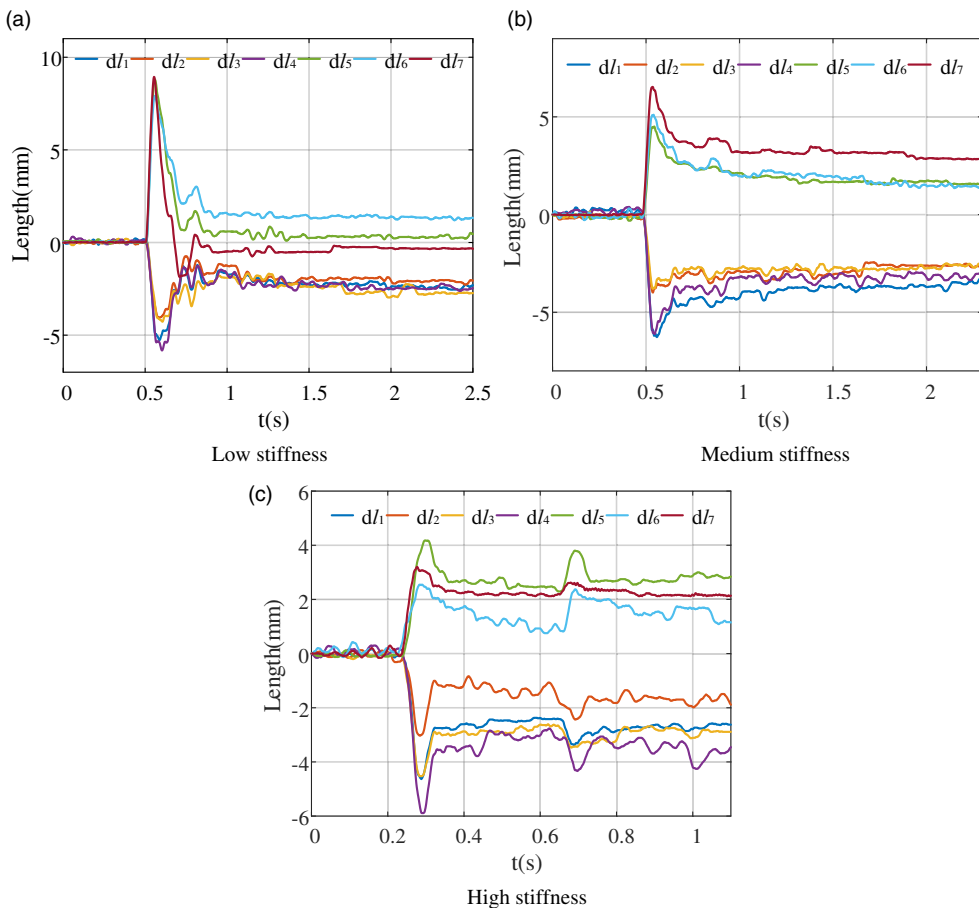
**Figure 22.** *Stiffness experiment show.*



**Figure 23.** *Experimental data of fixed-point stiffness.*

high. As mentioned earlier, the stiffness conditions were adjusted by planning different threshold values of cable forces to alter the stiffness characteristics of PCUR, where low stiffness: $\tau = [12.22, 13.35, 13.35, 12.22, 16.20, 16.20, 24.48]$, medium stiffness: $\tau = [21.10, 22.83, 22.83, 21.10, 25.68, 25.68, 38.81]$, and high stiffness: $\tau = [46.99, 50.49, 50.49, 46.99, 53.34, 53.34, 80.60]$. The experimental results are shown in Figure 23, where $dl_i$ refers to the amount of small change in the length of the ith cable.

(a), (b), and (c) give the amount of length change of seven cables for low, medium, and high stiffness conditions, respectively. The experimental results show that under low stiffness conditions, the absolute value of the variation in each cable length is within a range of 10 mm. Under moderate stiffness conditions, the absolute value of the variation in each cable length is within a range of 8 mm. Under high stiffness conditions, the absolute value of the variation in each cable length is within a range of 6 mm. Therefore, as the PCUR stiffness value increases, it becomes more difficult for external force to alter the position of the MP, thus making the motion of PCUR more stable, which aligns with the expected effect. However, providing the robot with excessive stiffness would compromise some aspects of human-robot interaction. In practical applications, it is advisable to increase stiffness as much as possible while ensuring flexibility in order to enhance motion stability while maintaining human-robot interaction. This ultimately improves the performance of PCUR.

## 7. Conclusion

The selection of the CGM and the stiffness characteristics have significant implications for the performance of PCUR. Compared with the conventional CGM based on eyelets and pulleys, the S-CGM proposed in this paper reduces the sliding friction on the cable with better accuracy and improves the reconfigurability of the PCUR. A precise kinematic model has been established based on S-CGM, errors have been analyzed, the continuity of the cable trajectory and tension has been demonstrated, and assurance for the continuity and stability of PCUR motion has been provided. Through simulation analysis of CGM, the maximum error of S-CGM is found to be only 2.7%, which is lower than that of the pulley-based CGM. Meanwhile, in order to further improve the motion stability of PCUR, this paper carries out the theoretical analysis of stiffness, establishes the mathematical model of stiffness, and develops the simulation model of PCUR. Through the stiffness simulation, we determined that the stiffness characteristics of PCUR can be achieved by adjusting the tension of the cable. Based on the stiffness experiments, we conclude that the motion of the PCUR becomes more stable when a higher stiffness is applied.

For future work, two main aspects require further research:

1. Investigation into the precise kinematics of S-CGM considering cable sag.

2. Establish the correlation between stiffness conditions and training modalities and design a user interaction interface to dynamically adjust stiffness conditions based on the patient's rehabilitation training needs, thereby enhancing the effectiveness of rehabilitation training.

## References

[1] J. B. Emelia, P.Muntner, A. Alonso, M. S. Bittencourt, C. S. Callaway, A. P. Carson, A. M. Chamberlain, A. R. Chang, S. Cheng, S. R. Das, F. N. Delling, L. Djousse, M. S. V. Djousse, J. F. Ferguson, M. Fornage, J. F. Jordan, S. S. Khan, B. M. Kissela, K. L. Knutson, T. W. Kwan, D. T. Lackland, T. T. Lewis, J. H. Lichtman, C. T. Longenecker, M. S. Loop, P. T. Lutsey, S. S. Martin, K. Matsushita, A. E. Moran, M. E. Mussolino, M. O'Flaherty, A. Pandey, A. M. Perak, W. D. Rosamond, G. A. Roth, U. K. A. Sampson, G. M. Satou, E. B. Schroeder, S. H. Shah, N. L. Spartano, A. Stokes, D. L. Tirschwell, C. W. Tsao, M. P. Turakhia, L. B. VanWagner, J. T. Wilkins, S. S. Wong, S. S. Virani and American Heart Association Council on Epidemiology and Prevention Statistics Committee and Stroke Statistics Subcommittee,

"Heart disease and stroke statistics-2019 update: A report from the American heart association," *Circulation* **139**(10), e56–e528 (2019).

[2]   M. W. McDonald, S. E. Black, D. A. Copland, D. Corbett, R. M. Dijkhuizen, T. D. Farr, M. S. Jeffers, R. N. Kalaria, F. Karayanidis, A. P. Leff, J. Nithianantharajah, S. Pendlebury, T. J. Quinn, A. N. Clarkson and M. J. O'Sullivan, "Cognition in stroke rehabilitation and recovery research: Consensus-based core recommendations from the second stroke recovery and rehabilitation roundtable," *Int J Stroke* **14**(8), 774–782 (2019).

[3]   M. Gittler and A. M. Davis, "Guidelines for adult stroke rehabilitation and recovery," *JAMA* **319**(8), 820 (2018).

[4]   C. M. Stinear, C. E. Lang, S. Zeiler and W. D. Byblow, "Advances and challenges in stroke rehabilitation," *Lancet Neurol* **19**(4),348–360 (2020).

[5]   V. S. Huang and J. W. Krakauer, "Robotic neurorehabilitation: A computational motor learning perspective," *J NeuroEng Rehabil* **6**(1), 5 (2009).

[6]   J. Mehrholz, M. Pohl, T. Platz, J. Kugler and B. Elsner, "Electromechanical and robot-assisted arm training for improving activities of daily living arm function, and arm muscle strength after stroke," *Cochrane Database of Syst Rev* (2015). doi: 10.1002/14651858.cd006876.pub4.

[7]   J. Laut, M. Porfiri and P. Raghavan, "The present and future of robotic technology in rehabilitation," *Curr Phys Med Rehabil Rep* **4**(4), 312–319 (2016).

[8]   M. Gouttefarde, J. Lamaury, C. Reichert and T. Bruckmann, "A versatile tension distribution algorithm for -DOF parallel robots driven by n+2 cables," *IEEE Trans Robot* **31**(6), 1444–1457 (2015).

[9]   H. Liu, C. Gosselin and T. Laliberté, "Conceptual design and static analysis of novel planar spring-loaded cable-loop-driven parallel mechanisms," *J Mech Robot* **4**(2), 021001 (2012).

[10]  D. Zanotto, G. Rosati, S. Minto and A. Rossi, "Sophia-3: A semiadaptive cable-driven rehabilitation device with a tilting working plane," *IEEE Trans Robot* **30**(4), 974–979 (2014).

[11]  S. Mengli, O. Yiming, J. Hu, C. Zhenyi, W. Changyang, L. Jiyu, X. Min, L. Weihua, W. Liu and Z. Shiwu, "A soft-packaged and portable rehabilitation glove capable of closed-loop fine motor skills'," *Nat Mach Intell* **5**(10), 1149–1160 (2023).

[12]  M. Khadem, F. Inel, G. Carbone and A. Slimane Tich Tich, "A novel pyramidal cable-driven robot for exercising and rehabilitation of writing tasks'," *Robotica* **41**(11), 3463–3484 (2023).

[13]  R. Zhang, D. Xie, C. Qian, X. Duan and C. Li, "Design of a flexible robot toward transbronchial lung biopsy'," *Robotica* **41**, 1055–1065 (2023).

[14]  A. Rodriguez-Barroso, M. Khan, V. Santamaria, E. Sammarchi, R. Saltaren and S. Agrawal, "Simulating underwater human motions on the ground with a cable-driven robotic platform," *IEEE Trans Robot* **39**(1), 783–790 (2023).

[15]  J.-B. Izard, M. Gouttefarde, M. Michelin, O. Tempier and C. Baradat, "A Reconfigurable Robot for Cable-Driven Parallel Robotic Research and Industrial Scenario Proofing," **In:** *Mechanisms and Machine Science. Cable-Driven Parallel Robots*, (Springer, 2013) pp. 135–148.

[16]  C. Sturm, L. Wildan and T. Bruckm, "Wire robot suspension systems for wind tunnels," *Wind Tunnels Experim Fluid Dyn Res* **2**, 30–50 (2012).

[17]  T.-L. N.-D. MartinJ.-D. Otis, T. Laliberté, D. Ouellet, D. Laurendeau and C. Gosselin, Cable tension control and analysis of reel transparency for 6-DOF haptic foot platform on a cable-driven locomotion interface. CERN european organization for nuclear research – zenodo, (2009).

[18]  J. Lenarčič and M. Stanišić, *Advances in Robot Kinematics: Motion in Man and Machine* (Springer, 2010).

[19]  A. Fattah and S. K. Agrawal, "On the design of cable-suspended planar parallel robots," *J Mech Design* **127**(5), 1021–1028 (2005).

[20]  J. Pusey, A. Fattah, S. Agrawal and E. Messina, "Design and workspace analysis of a 6-6 cable-suspended parallel robot," *Mech Mach Theory* **39**(7), 761–778 (2004).

[21]  S. Kawamura, W. Choe, S. Tanaka and S. R. Pandian, "Development of an Ultrahig Speed Robot FALCON Using Wire Drive System," **In:** *Proceedings of 1995 IEEE International Conference on Robotics and Automation* (2002) pp. 215–220.

[22]  Y. X. Su, B. Y. Duan, R. D. Nan and B. Peng, "Development of a large parallel-cable manipulator for the feed-supporting system of a next-generation large radio telescope," *J Robotic Syst* **18**(11), 633–643 (2001).

[23]  S. Fang, D. Franitza, M. Torlo, F. Bekes and M. Hiller, "Motion control of a tendon-based parallel manipulator using optimal tension distribution," *IEEE/ASME Trans Mechatron* **9**(3), 561–568 (2004).

[24]  H. Vallery, J.von Z. Lutz, G. Rauter, M. Fritschi, C. Everarts, R. Ronsse, A. Curt and M. Bolliger, "Multidirectional Transparent Support for Overground Gait Training," **In:** *IEEE 13th International Conference on Rehabilitation Robotics (ICORR)*, (2013) pp. 1–7.

[25]  H. Jamshidifar, A. Khajepour, B. Fidan and M. Rushton, "Kinematically-constrained redundant cable-driven parallel robots: Modeling, redundancy analysis, and stiffness optimization," *IEEE/ASME Trans Mechatron* **22**(2), 921–930 (2017).

[26]  T. Bruckmann, L. Mikelsons, T. Brandt, M. Hiller and D. Schramm, "Wire Robots Part I: Kinematics, Analysis & Design," **In:** *Parallel Manipulators, New Developments* (2012).

[27]  A. Renfrew, "Book review: Introduction to robotics: Mechanics and control," *Int J Electr Eng Educ* **41**(4), 388–388 (2004).

[28]  S. Macfarlane and E. A. Croft, "Jerk-bounded manipulator trajectory planning: Design for real-time applications," *IEEE T Robotic Autom* **19**(1), 42–52 (2003).

[29]  R. Verhoeven, Analysis of the workspace of tendon-based stewart platforms advance access published July, (2004).

[30]  W. Kraus and A. Pott, "Scenario-Based Dimensioning of the Actuator of Parallel Cable-Driven Robots," **In:** *New Trends in Mechanism and Machine Science, Mechanisms and Machine Science*, (Springer, 2013) pp. 131–139.

[31]  R. Verhoeven, M. Hiller and S. Tadokoro, "workspace, Singularities and Classification of Tendon-Driven Stewart Platforms," **In:** *Advances in Robot Kinematics: Analysis and Control*, (1998) pp. 105–114.

[32] Z. Cui and X. Tang, "Analysis of stiffness controllability of a redundant cable-driven parallel robot based on its configuration," *Mechatronics* **75**, 102519 (2021).

[33] V. Ferravante, E. Riva, M. Taghavi, F. Braghin and T. Bock, "Dynamic analysis of high precision construction cable-driven parallel robots," *Mech Mach Theory* **135**, 54–64 (2019).

[34] L. Mikelsons, T. Bruckmann, M. Hiller and D. Schramm, "A Real-Time Capable Force Calculation Algorithm for Redundant Tendon-Based Parallel Manipulators," **In:** *2008 IEEE International Conference on Robotics and Automation*, (2008).

[35] W. B. Lim, S. H. Yeo and G. Yang, "Optimization of tension distribution for cable-driven manipulators using tension-level index," *IEEE/ASME Trans Mechatron* **19**(2), 676–683 (2014).

[36] M. Gouttefarde, J. Lamaury, C. Reichert and T. Bruckmann, "A versatile tension distribution algorithm for n-DOF parallel robots driven by n+2 cables," *IEEE Trans Robot* **31**(6),1444–1457 (2015).

[37] Y.-L. Wang, K.-Y. Wang, Y.-J. Chai, Z.-J. Mo and K.-C. Wang, "Research on mechanical optimization methods of cable-driven lower limb rehabilitation robot," *Robotica* **40**(1), 154–169 (2022). doi: 10.1017/S0263574721000448.